Journal of Himalayan Earth Sciences 40 (2007) 51-66

Hydrochemical characterization and numerical simulation of fluid flow in a compressional tectonic environment

M. Asim Yousafzai
Department of Geology, University of Peshawar, Peshawar

Abstract

Groundwater samples were analyzed from springs and wells as part of a larger program of investigations in a compressional tectonic environment. The study site covers the Peshawar Basin and its surroundings in the Himalayan foothills which is experiencing a tectonic compression of 90 Mpa because of the ongoing India - Eurasia collision. The study area extends from Main Karakoram Thrust (MKT) and Main Mantle Thrust (MMT) in the north, through Main Central Thrust (MCT) and Main Boundary Thrust (MBT) in the center to Salt Range Thrust (SRT) in the south. The study area can be divided into two hydrogeological domains. Springs with normal (< 20^{o}C) and anomalously high temperatures (up to 68^{o}C) are abundant in the northern part of the study area while the southern part is divided into isolated basins with a number of drilled wells and dug-wells. Hydrochemical signatures of elevated strontium (Sr), SiO_2, boron (B) - and the geothermometric signatures - all indicate a deep circulation of the emerging groundwater. Moreover, for several of the sampling sites, analyzed water compositions, measured spring and water well temperatures, and reservoir temperatures calculated for spring waters, all point to waters that are anomalous in both chemistry and temperature. These characteristics suggest origin of the anomalous waters from deep horizons within the basin. Remarkable proximity of all the thermal and hydrochemical anomalies to major mapped faults suggests that the anomalous waters ascended along these faults from greater depths. The Peshawar intermontane basin is a broad, oval shaped depression comprising of a thick sequence of lacustrine, deltaic and fluvial sediments overlain by loess and alluvial deposits. The basin was divided into four hydrostratigraphic units in order to perform numerical simulations using the 3-D finite-element (FEMWATER) module of Groundwater Modeling System (GMS). Pressure head data generated by the numerical simulations have been compared with the field measurements of hydraulic heads. Results of the transient simulations indicate that topography alone is not sufficient to induce the pressure heads observed in the field, generating consistently positive residuals, ranging 0.98-2.90 m over the topography-driven flow. The positive residuals disappeared after inclusion of the elastic properties of the four hydrostratigraphic units in the model, suggesting the additional effect of tectonic compression on subsurface water flow.

1. Introduction

Foreland basins, such as the Himalayan foredeep, characterized by stratigraphic continuity, typically host large groundwater flow systems. Because groundwater flow is the dominant mechanism for transporting chemical mass in sedimentary basins, knowledge of the hydrodynamics and geochemistry of flow and transport is a fundamental prerequisite to understanding geologic processes (Garven, 1995). Such tectonically driven fluids play an important role in the processes of faulting, magmatic activity, migration of hydrocarbons, mineral transport, metamorphism and paleomagnetism (Oliver, 1986).

The objective of this research is to gain understanding of the hydrotectonic processes operating in the Himalayan foreland fold-and-thrust belt, by field-testing the hypothesis that tectonic compression generates abnormally high hydrostatic pressures on top of the topography-driven heads in an intermontane sedimentary basin. The research addresses three aspects of the groundwater from the study area: field characteristics (e.g. distribution of anomalously warm or hot springs in relation to the faultlines), hydrochemical signatures and model hydrodynamic behavior. This research has provided tests of the hypothesis, and also quantified the tectonically-driven overpressure only postulated thus far in theoretical treatment of the subject from topography driven head (e.g.: Oliver, 1986; Deming et al., 1990; Ge and Garven, 1994; Bitzer et al., 1996; Neuzil, 1995; McPherson and Garven, 1999). It is important to note that Garven and others postulated such transient overpressure while working on the ancient Arkoma Basin whereas this work is being done in a basin that is still under present-day tectonic stress. This study is considered to be the first field attempt to identify the effects of ongoing tectonic stress on the groundwater flow patterns in currently active compressional tectonic regimes.

The study site covers the Peshawar Basin and its surroundings in the Himalayan foreland fold-and-thrust belt of Pakistan (Fig. 1). The area, located between latitudes 32°N–37°N and longitudes 70°E–74°E, is characterized by steep topography and U-shaped glaciated valleys in the north, which are drained by the River Indus entering from Indian Kashmir and the River Kabul entering from Afghanistan.

2. Tectonic framework

The ongoing northward convergence of the Indian plate with greater Asia has resulted in the formation of four major south-verging thrust faults striking the length of the Himalayan arc (Fig. 2). The northernmost of the four main thrusts is Main Karakoram Thrust (MKT), which separates Asian plate metasedimentary rocks from the Kohistan island arc (KIA). The Main Central Thrust (MCT) emerges along the southern edge of the High Himalaya, has not been observed to break Quaternary deposits, and is, therefore, considered to be inactive (Nakata, 1989). The Main Mantle Thrust (MMT) separates the KIA from rocks of the Indian continental margin. The Main Boundary Thrust (MBT), marking the southern edge of the Lesser Himalaya, is expressed in bedrock along the arc and is locally observed to displace Quaternary deposits. The southernmost thrust is the Salt Range Thrust (SRT), which separates rocks of the Indian continental shelf from the Quaternary alluvium of the Indus plain (Pivnik and Sercombe, 1993). It is considered to be the most active of the four thrusts and delineates the northern limit of the exposed Indian Plate.

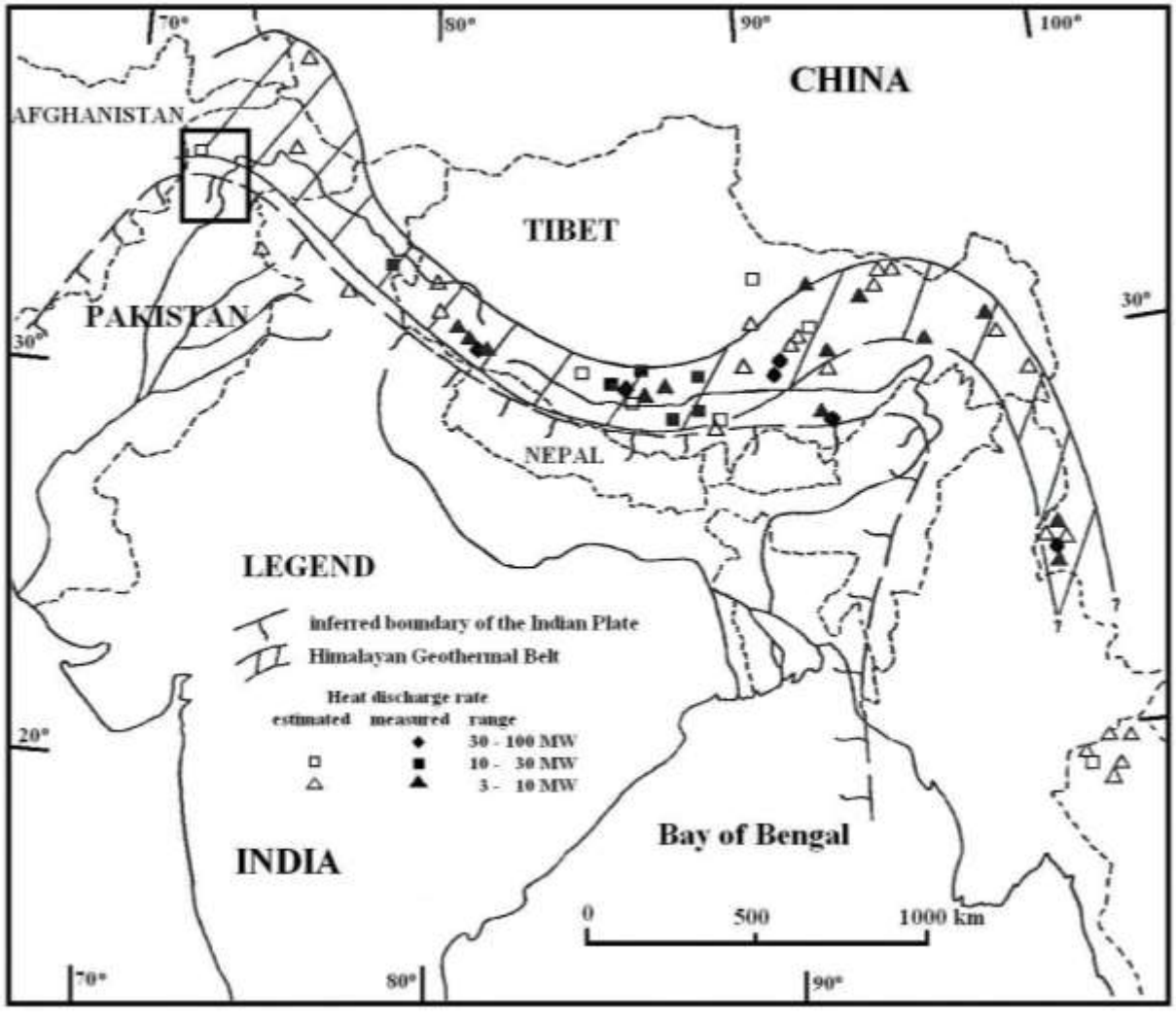

Fig. 1. Regional map with boxed area showing the location of the study area (after Hochstein and Yang, 1995).

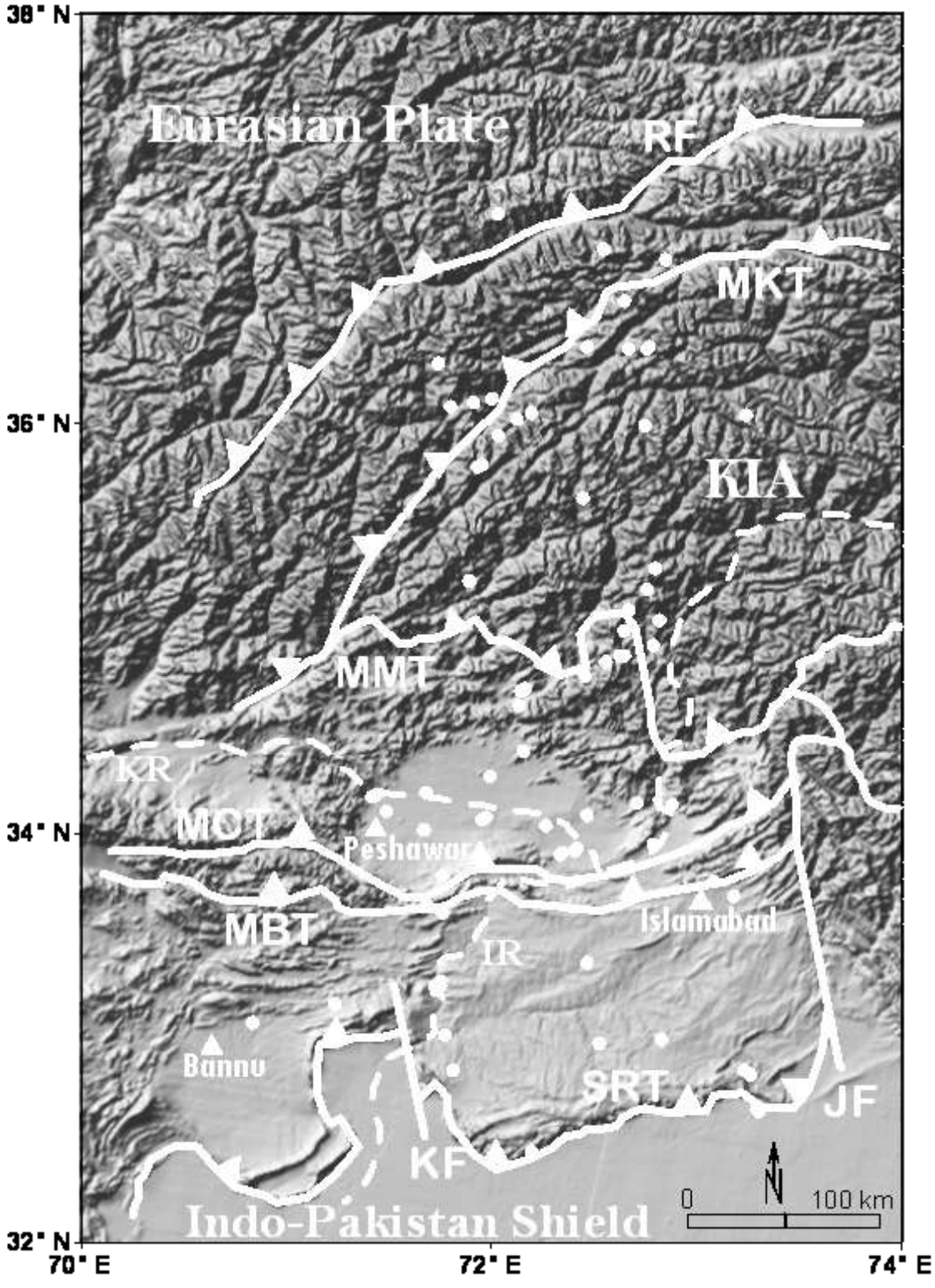

Fig. 2. Map of the major faults and sampling sites (white dots) superimposed on the shaded relief map of the study area. Salt Range Thrust (SRT); Main Boundary Thrust (MBT); Kalabagh Fault (KF); Main Central Thrust (MCT); Main Mantle Thrust (MMT); Jhelum Fault (JF); Main Karakoram Thrust (MKT); Indus River (IR); Kabul River (KR); Kohistan Island Arc (KIA); Reshun Fault (RF).

3. General hydrogeology

The Peshawar intermontane basin is surrounded by the Precambrian and Tertiary intrusive and metamorphic rocks on the north and sedimentary rocks of Paleogene and Neogene to the south (Fig. 3). It is a broad, oval shaped depression comprising of a thick sequence of lacustrine, deltaic and fluvial sediments overlain by loess and alluvial deposits dated at 2.8 to 0.6 Ma (Hussain et al., 1998). These sediments, consisting mainly of sand and gravel, form productive aquifers in the north and south of the basin. However, in the central part, the coarse sediments are interbedded with clay, silt and sandy silt, attaining its maximum thickness and providing semi-confinement for a number of aquifers. Depth to the water table is less than 5 m, except on the margins of the basin and in the southeast where it ranges from 5 to more than 30 m. Hydraulic conductivity in the basin ranges from 30-60 m/day and average specific yield is 12%. These values indicate a potentially high-yielding aquifer with substantial storage capacity (Rathur, 1987). The main sources of recharge to the aquifer are precipitation, seepage from rivers, surface storage reservoirs, and irrigation networks. A large number of drilled wells and dug wells are present in the area. Drilled wells range in depth from 50 to 150 m whereas dug wells are up to 20 m in maximum depth. Water table elevation varies considerably in the area. It ranges from less than 100 m in the southern portion to more than 1500 m in the mountainous north (in relation to the mean sea level).

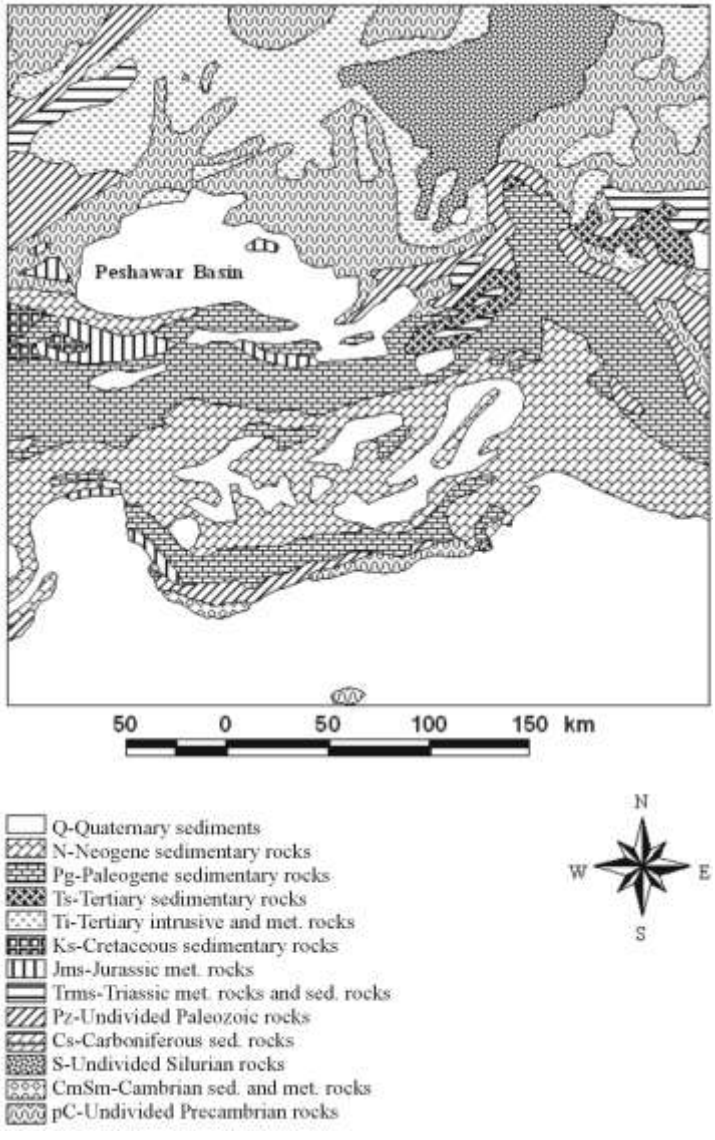

Fig. 3. Geologic map of the southern part of the study area showing prominent lithologies (Modified after Wandrey and Law, 1999).

4. Tools and procedures

A total of two sets of 71 water samples were collected during July-August 2003 from water wells, springs and seepages throughout the study area. General physico-chemical parameters such as temperature, pH, Total Dissolved Solids (TDS), and electrical conductivity (EC), were determined in the field using Technika Water Quality Meter 850081 with dedicated sensor probes. All the water samples were filtered with a 0.45 µm pore diameter filter, and samples for cation analyses were acidified with nitric acid. Water samples were analyzed for major and trace elements (Tables 1-3) at Kent State University. Cations were analyzed using Perkin Elmer Optima 3300 DV ICP-OES with an AS90 Plus autosampler. Precision errors were less than ±6% for trace elements and less than ±3% for the major cations (95% confidence). Anion concentrations were determined using DIONEX DX 120 Ion Chromatograph with an AS50 autosampler. Precision errors were less than ±3% for all the anions (95% confidence). Bicarbonate ion (HCO_3^-) was indirectly derived from total carbon analyzed by SHIMADZU TOC 5000 instrument with precision error less than ±2% (95% confidence). The charge balance (cations-anions/cations+anions) was less than ± 5% for all the samples.

Each sampling site was mapped with a Garmin GPS V with a position accuracy of less than ±3 m. The sampling sites ranged in elevation from 198 to 2472 m above MSL. Each sampling site was mapped using Garmin GPS V, with a position accuracy of less than ±3 m. In addition, surface infiltration rates were measured at a number of sites using a double-ring infiltrometer. The 3D numerical model was constructed from the field data collected during the sampling program in summer 2003. The regional groundwater flow in the study area was numerically simulated using U.S. Department of Defense commercial software "Groundwater Modeling System (GMS v 5.1)".

5. Hydrochemistry

The analyses were plotted on discriminant diagrams of Piper (1944) (Fig. 4). The spring waters have been divided into three groups: Ca-Mg-HCO_3 waters, Ca-Mg-SO_4 waters, and Na-SO_4-Cl waters. Ca, Mg, HCO_3 or SO_4 ions are dominant in most of the spring waters. The predominance of Ca-Mg-HCO_3 – type waters suggest that the fluids interacted with carbonate minerals and have not been significantly altered by cation exchange, dissolution of evaporites, and/or mixing with more evolved waters. However, water from two springs (S2 and S16) exhibit (Na+K) > Ca > Mg, with sulfate for the dominant anion (Fig. 4) and both emerge at an anomalously high temperatures. Sample S2 is 6 °C over the mean annual ground surface temperature, and sample S16 is the hot spring of Garam Chashma with a temperature of 67°C, i.e. 52°C over the mean annual ground surface temperature for this location. Similarly, most of the samples from shallow-dug wells are predominantly Ca-HCO_3 type, with a few exceptions, where none of the cations is especially dominant (Fig. 4). Water samples from deep wells can be divided into two groups: Ca-Mg-HCO_3 waters and Na-HCO_3 waters (Fig. 4). Aside from the major ions, nitrate concentrations reported in Tables 1-3 may be almost certainly attributed to surface pollutants (e.g. fertilizers, domestic waste). Concentrations may also be increased by evaporation under hot, arid conditions.

All samples exhibit temperatures of at least 6°C above the local mean annual temperature (Tables 1-3). Furthermore, all such samples with significant excess temperature (> 6°C) over the local mean annual air temperature also exhibit anomalously high concentrations of SiO_2, whereas those along the MKT are characterized by anomalously high concentrations of boron and strontium (Tables 1-3). The occurrence of strontium in groundwater is commonly attributed to diagenesis of aragonite, rich in Sr^{+2} which is idiomorphically replacing Ca^{+2}. During diagenesis, when aragonite is converted to the more stable polymorph calcite, the strontium is released to water. Fig. 5 shows, indeed, good correlation between the concentrations of Sr and Ca in spring waters; however in some high-silica springs with anomalously elevated temperatures and located between MKT and RF faultlines (see Fig. 2) there is also a good correlation between the concentrations of Sr and SiO_2. Evans et al. (2001) reported occurrence of radiogenic Sr from hydrothermal sources in some Nepalese rivers. It is, therefore, postulated that Sr in the spring waters emerging from the granitic complex north of Peshawar Basin is of hydrothermal origin.

Fig. 6 clearly demonstrates that boron concentrations in spring waters from the study area are closely associated with the igneous complex, and perhaps with the geothermal activity. The salinity of the spring water has been demonstrated by using the calibrated symbol sizes at Piper's plots (see Fig. 4). The (Na+K) vs Cl plot (Fig. 7) indicates that the high salinity cannot be attributed to simple dissolution of NaCl, as there is much more Na than Cl (roughly for every 20 meq/l of Cl there is 50 meq/l of Na+K). The most obvious source for the excess Na+K would be dissolution of feldspars, but that would require higher temperatures further implied by the hydrochemical geothermometers. Lastly, a number of water samples from springs and drilled wells fall significantly off the typical carbonate dissolution lines on Fig. 8. Several spring water samples, e.g. S7, S23, S5 and S2 show substantial excess of (Ca+Mg). Examination of Table 3 indicates that Mg is the dominant cation in these samples, suggesting dissolution of chlorites. Such high concentrations of HCO_3 can be attributed only to mixing with deep subsurface brines ascending via nearby SRT (see Fig. 2).

Table 1. Hydrochemical data for ground water samples from drilled water wells (ionic concentrations in mg/l).

Sample ID	pH	T °C	EC (µS/cm)	Ca	Mg	Na	K	Cl	NO_3	SO_4	HCO_3	SiO_2	Sr	B	Li	ΔT °C
W1	7.3	30	1210	127.8	42.5	54.4	3.3	147.1	168.5	148.6	198.3	21.3	1.355	0.471	0.02	6.3
W2	7.0	27	1015	92.7	47.7	83.2	5.1	51.9	39.9	299.4	331.1	19.2	1.348	0.361	0.11	3.4
W3	8.2	27	8280	59.4	115.4	1934.7	34.2	1168.9	463.6	1760.7	1855.9	26.2	0.412	0.131	0.02	3.8
W4	7.8	28	1150	38.4	49.5	170.9	10.8	35.2	14.5	202.0	580.9	24.4	0.986	0.200	0.03	4.8
W5	7.7	25	391	45.0	17.1	18.7	9.6	12.5	4.9	66.5	181.3	12.3	0.626	0.054	0.02	5.1
W6	7.9	28	2640	75.7	71.3	375.4	12.8	422.4	30.0	578.8	343.5	18.3	1.973	0.993	0.11	5.7
W7	7.9	26	938	23.7	38.2	137.6	4.8	52.8	85.7	78.6	395.3	27.5	0.131	0.130	0.03	3.1
W8	8.6	29	4760	6.9	5.1	1162.9	19.4	738.9	123.5	1020.5	1025.5	10.1	0.254	0.862	0.07	6.1
W9	7.9	29	254	32.3	10.4	63.7	8.5	11.9	6.1	57.9	165.1	11.8	0.288	0.442	0.01	3.9
W10	8.0	28	1736	71.7	68.1	187.5	13.1	270.7	71.9	202.0	373.9	22.2	0.908	0.553	0.05	2.9
W11	7.7	29	621	43.7	15.5	30.4	2.2	21.6	22.6	31.4	196.9	19.9	0.409	0.442	0.01	6.9
W12	7.5	28	962	78.0	42.3	63.5	6.4	71.9	119.8	73.0	335.4	24.5	0.113	0.333	0.13	5.9
W13	7.7	30	380	41.4	11.8	20.2	2.7	6.6	27.4	11.6	210.0	32.1	0.156	0.322	0.01	6.6
W14	7.6	29	632	57.6	27.1	37.6	4.8	48.6	36.0	85.0	225.1	17.1	0.804	0.000	0.03	7.3
W15	7.4	25	680	65.9	21.3	40.8	2.4	72.4	97.4	63.3	161.9	16.9	0.611	0.000	0.01	6.2
W16	7.5	27	530	38.1	16.2	56.3	4.3	14.2	16.0	32.3	285.4	25.8	0.446	0.000	0.02	4.4
W17	7.5	27	801	106.6	19.2	33.7	3.3	62.3	114.0	81.6	163.2	32.5	0.809	0.000	0.04	7.6
W18	7.3	29	1137	75.8	51.8	84.8	3.3	111.2	36.1	228.7	280.3	23.7	1.880	0.060	0.10	4.8
W19	7.7	29	856	68.2	53.6	32.7	7.6	16.5	12.9	187.5	338.5	18.0	1.351	0.000	0.03	4.9
W20	7.5	25	426	66.9	7.7	11.5	4.4	5.5	12.7	44.7	221.3	18.0	0.301	0.000	0.01	6
W21	7.7	27	498	23.1	15.5	71.5	3.4	19.1	10.0	113.6	201.6	15.3	0.225	0.000	0.01	5.7

T_{NaCaK} °C: Source reservoir temperature determined by the cation geothermometer (Mg-corrected Na Ca K)
$T_{Chaledony}$ °C: Source reservoir temperature determined by the chalcedony geothermometer
$T_{Mg\text{-}Li}$ °C: Source reservoir temperature determined by the Mg-Li geothermometer
ΔT °C: Difference between water sample temperature and mean annual ground surface temperature at the location

Table 2. Hydrochemical data for ground water samples from dug water wells (ionic concentrations in mg/l).

Sample ID	pH	T °C	EC (µS/cm)	Ca	Mg	Na	K	Cl	NO_3	SO_4	HCO_3	SiO_2	Sr	B	Li	ΔT °C
D1	8.1	28	896	45.0	33.0	124.8	11.1	70.0	3.1	395.8	140.6	15.1	0.988	0.224	0.02	3.4
D2	7.7	29	1495	74.0	89.7	89.1	13.7	205.2	110.9	295.6	261.8	21.6	0.421	0.066	0.03	6.1
D3	7.6	28	431	79.6	24.3	25.7	4.2	25.9	53.4	121.3	195.6	22.8	0.327	0.030	0.01	5.1
D4	7.9	29	328	29.0	11.9	26.4	4.8	8.5	14.3	13.8	183.0	24.0	0.266	0.000	0.01	5.7
D5	7.7	28	297	18.3	10.3	27.6	5.7	11.2	10.2	15.2	152.3	20.2	0.258	0.000	0.01	4.7
D6	7.1	16	665	79.3	21.4	8.0	4.7	2.3	3.5	155.1	167.0	14.0	0.477	0.000	0.04	1.7
D7	7.5	24	885	86.8	52.7	54.5	11.1	66.0	6.0	253.0	261.9	18.1	0.602	0.000	0.05	1.2
D8	7.6	24	1061	57.2	63.5	110.6	13.8	25.9	6.7	429.2	360.6	19.5	1.298	0.146	0.04	1.3
D9	7.3	29	892	87.6	31.7	50.4	5.0	29.8	49.7	138.3	309.6	24.9	0.779	0.000	0.05	5.8
D10	7.4	26	504	54.0	23.7	20.6	2.5	15.1	17.9	87.4	202.9	17.5	0.343	0.000	0.02	6.6
D11	8.1	28	151	23.6	3.4	6.3	3.2	5.5	4.3	38.4	56.1	3.8	0.116	0.000	0.01	8.1
D12	7.4	28	561	63.1	15.3	19.6	3.6	23.5	4.6	42.0	221.9	21.3	0.291	0.000	0.00	5.5
D13	8.0	29	463	14.8	21.6	55.0	5.4	9.6	9.2	29.8	283.4	15.3	0.414	0.000	0.01	5.7
D14	7.7	27	522	81.6	10.3	9.3	2.4	11.1	8.2	11.1	225.3	21.7	0.323	0.000	0.00	6.4
D15	7.5	27	408	67.9	10.9	4.3	2.1	4.6	5.0	33.3	208.4	12.8	0.226	0.000	0.00	6.8
D16	7.3	26	1148	139.3	26.7	35.5	2.5	101.8	104.4	110.7	238.7	20.9	0.805	0.000	0.01	6.6

Table 3. Hydrochemical data for spring water samples (ionic concentrations in mg/l).

Sample ID	pH	T °C	*EC* (µS/cm)	Ca	Mg	Na	K	Cl	NO_3	SO_4	HCO_3	SiO_2	Sr	B	Li	ΔT °C
S1	7.4	25	718	71	32.4	36.5	5.6	25.9	15.3	182.1	218.7	14	0.84	0.15	0.18	1.4
S2	7.4	31	2940	138.1	95.8	439.3	5.2	342.4	79.7	972	353.1	18.1	1.92	0.39	0.17	5.9
S3	8.7	20	350	26.1	34.3	9.5	2.2	0.5	5.3	49.4	218.4	11.3	0.15	0	0.04	4.1
S4	8.2	21	479	39.1	58.4	22.5	3.6	1.3	6.3	183.3	271.4	12.2	1.05	0.46	0.06	5.2
S5	7.5	15	1184	195.9	95.8	14.6	3.9	1.5	2.4	798.9	96.5	12.5	0.22	0	0.08	-0.3
S6	7.6	21	625	100.2	56.4	29.1	11.7	1.2	4.5	475.6	107.5	14.7	1.99	0.12	0.07	5.5
S7	8.5	26	1520	147.5	147.4	86.9	10.9	7.5	3.9	971.6	275.7	20.6	2	0.45	0.16	10.7
S8	7.4	8	98	22.5	4.6	3.5	1.5	0.1	1.7	54.9	28.3	1.9	0.11	0	0	-7.6
S9	7.4	16	936	125.1	47.7	29.3	7.4	11.6	4	429.7	194	15.6	0.8	0.12	0.13	0.6
S10	7.8	16	907	93.1	81.4	29.1	9.5	0.7	6.7	425	307.5	10.5	1.04	0	0.05	0.7
S11	7.9	8	97	20.4	4.3	3.6	2	0.2	1.8	71.4	15.9	4.9	0.1	0	0	-7.7
S12	7.2	16	623	68	25.7	7.8	2.5	2.8	8.7	129.8	164.3	10.9	0.17	0	0.03	0.2
S13	8	16	430	38.6	9	44.9	4.6	47.7	3.3	116	80.2	8.9	0.27	0	0.03	0.1
S14	8.1	16	242	49.5	5.4	4.3	1.4	2.7	3.3	97.7	77	12	0.06	0	0	0
S15	7.9	10	57	11.6	1.2	3.1	1.2	0.5	2.6	12.9	29	5	0.04	0	0	-5.6
S16	7.3	67	885	39.4	2.1	170.9	8.5	25.1	3.5	366.1	128.3	53.5	0.53	0.69	1.94	52
S17	7.7	16	436	51.2	29.9	7.3	2.4	0.9	6.5	122.2	182.6	8.3	0.21	0	0.04	0.3
S18	7	18	639	66.7	20.6	20.2	5.2	25.7	5.2	102.9	164.7	8.9	0.32	0.49	0.21	2
S19	7.5	16	357	50.8	15.9	5.5	2.6	1.9	9.1	22.6	196.7	8.8	0.2	0	0.01	0.4
S20	7.5	16	405	54.6	26.7	5.2	2.6	1.9	7.6	64.5	200.8	7.9	0.25	0	0.01	0.3
S21	8.2	16	182	29.2	7.1	9	3.5	0.4	5.4	23.7	127.9	10.6	0.14	0	0.01	0.5
S22	7.3	27	527	59.3	23.5	15.8	1.8	17.3	36.2	74.1	219.4	15.7	0.44	0	0.01	7.7
S23	7.6	25	1475	266.7	55	58.4	11.5	12.4	4.8	962	145.8	29.3	1.9	0	0.03	5.7
S24	7.8	21	467	52	18.6	26.4	2.3	6.8	12.5	114.9	184.7	18.6	0.23	0	0.02	1.9
S25	7.6	22	559	95.4	29.1	14.8	3.4	8.5	7.8	252.1	178.3	20.9	0.73	0	0.02	2
S26	8.1	19	382	56.8	15.6	6.6	1.3	3.7	4.2	29.1	195.9	9.1	0.58	0.39	0.01	0.5
S27	7.3	20	584	82.5	15.8	13.7	4.7	18.3	52.6	56.1	208.3	49.6	0.33	0.44	0.02	1.2
S28	7.4	19	402	55.6	12.4	8.6	2.7	10.1	14.4	27.9	211.8	15.3	0.11	0	0.01	0.7
S29	7.3	21	457	72.6	3.1	4.5	0.5	6.2	11.2	5.4	156.6	18.3	0.18	0.44	0.05	3.7
S30	7.5	20	41	6.1	0.3	4.1	1	1.4	7.4	4.2	4.4	8.8	0.04	0	0	2.8
S31	7.8	20	396	42.2	24.5	6.9	1.1	3.1	16.7	9.5	249.5	31.8	0.25	0	0	2.6
S32	6.7	18	182	27.8	6.1	6.2	1.4	6.6	4.8	13	89.1	23.3	0.13	0.55	0	1.1
S33	7.2	18	227	30.4	9.8	7.8	2.2	6.3	17.3	12.5	113.3	24.5	0.14	0	0	1
S34	8.1	17	40	10.2	0.9	2.9	1.4	3.3	4	4.6	292.3	4.5	0.1	0	0	0.6

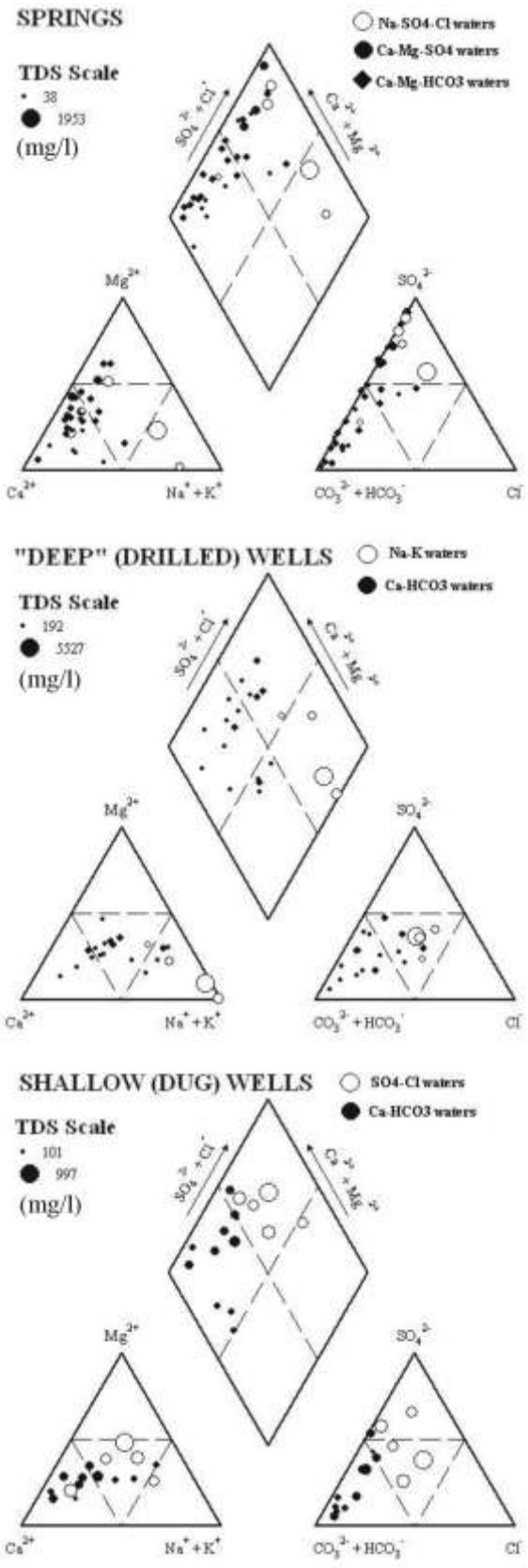

Fig. 4. Piper (1944) discriminant diagram for various types of waters.

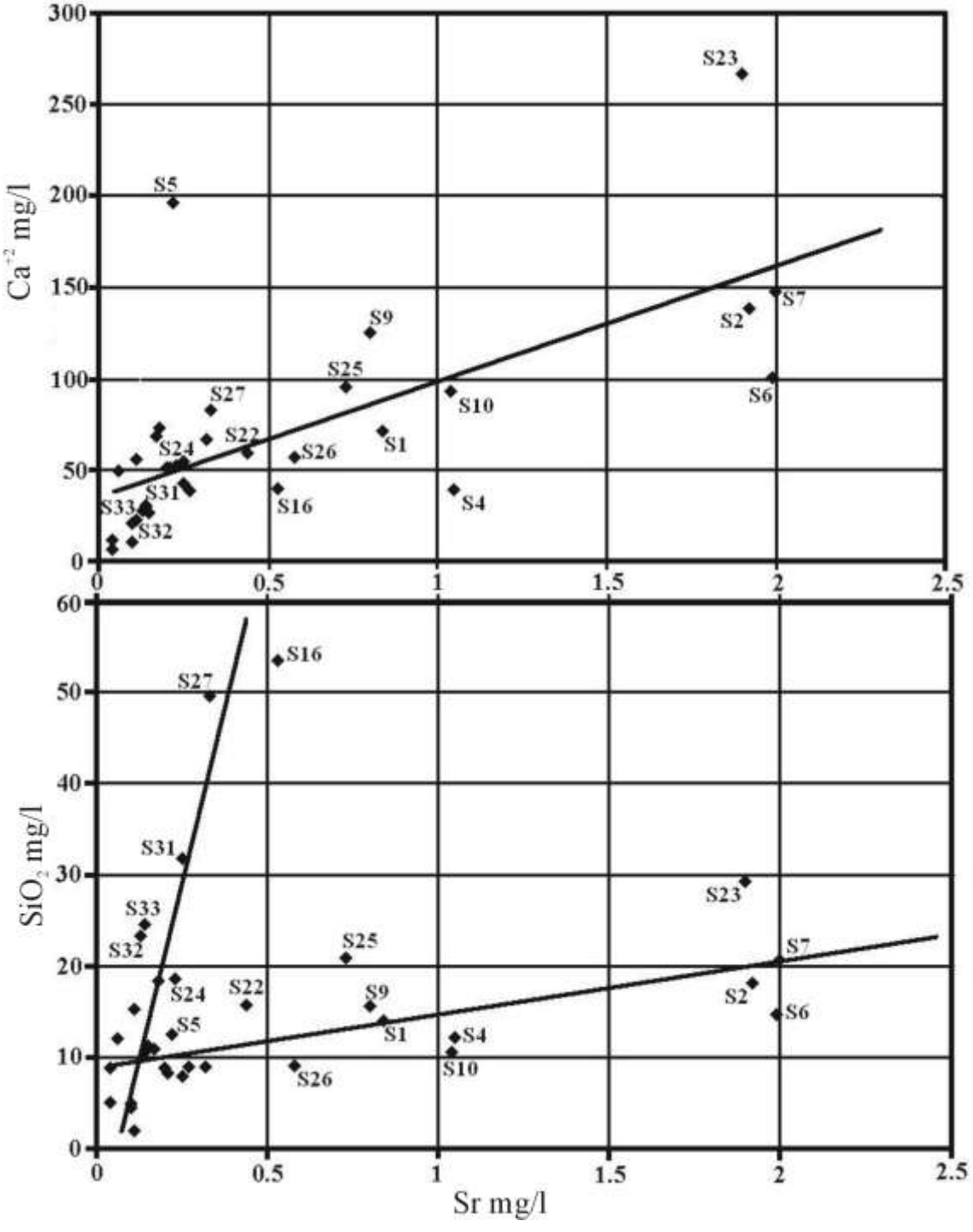

Fig. 5. Correlation between Sr and SiO_2 and Ca for spring waters.

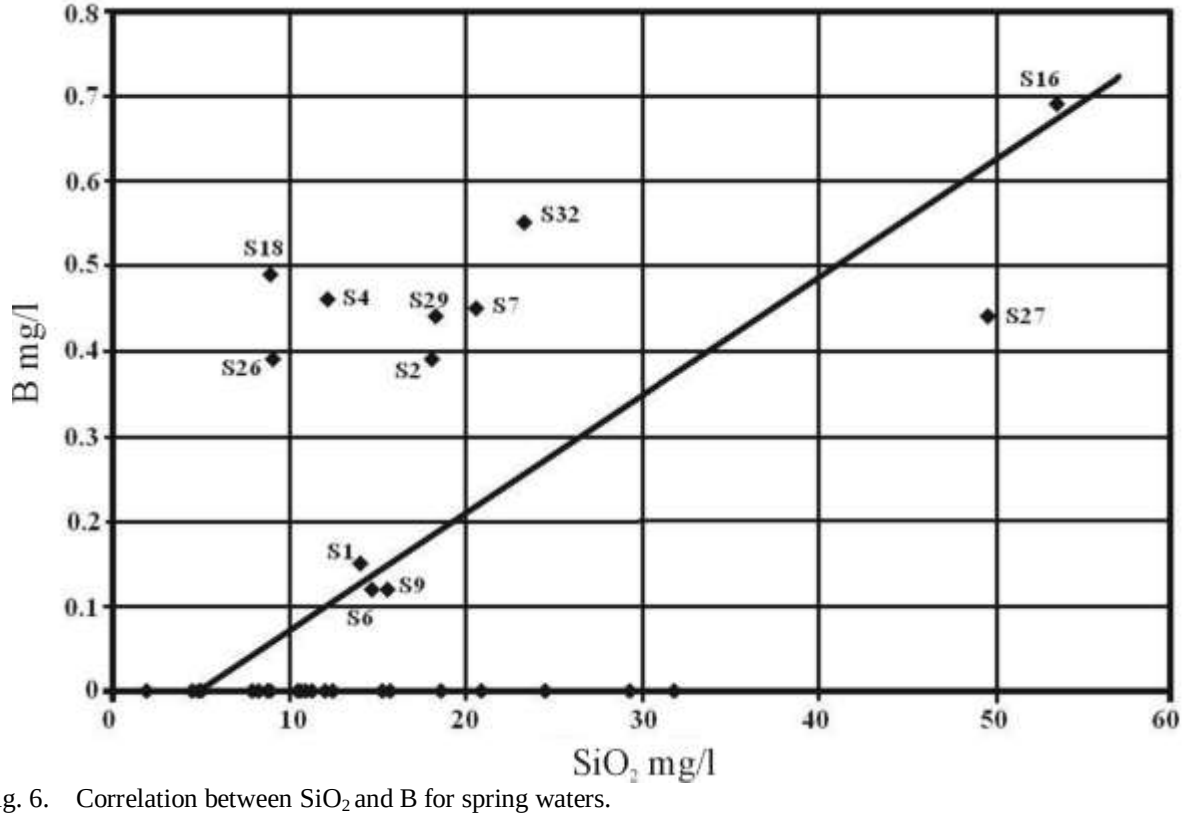

Fig. 6. Correlation between SiO_2 and B for spring waters.

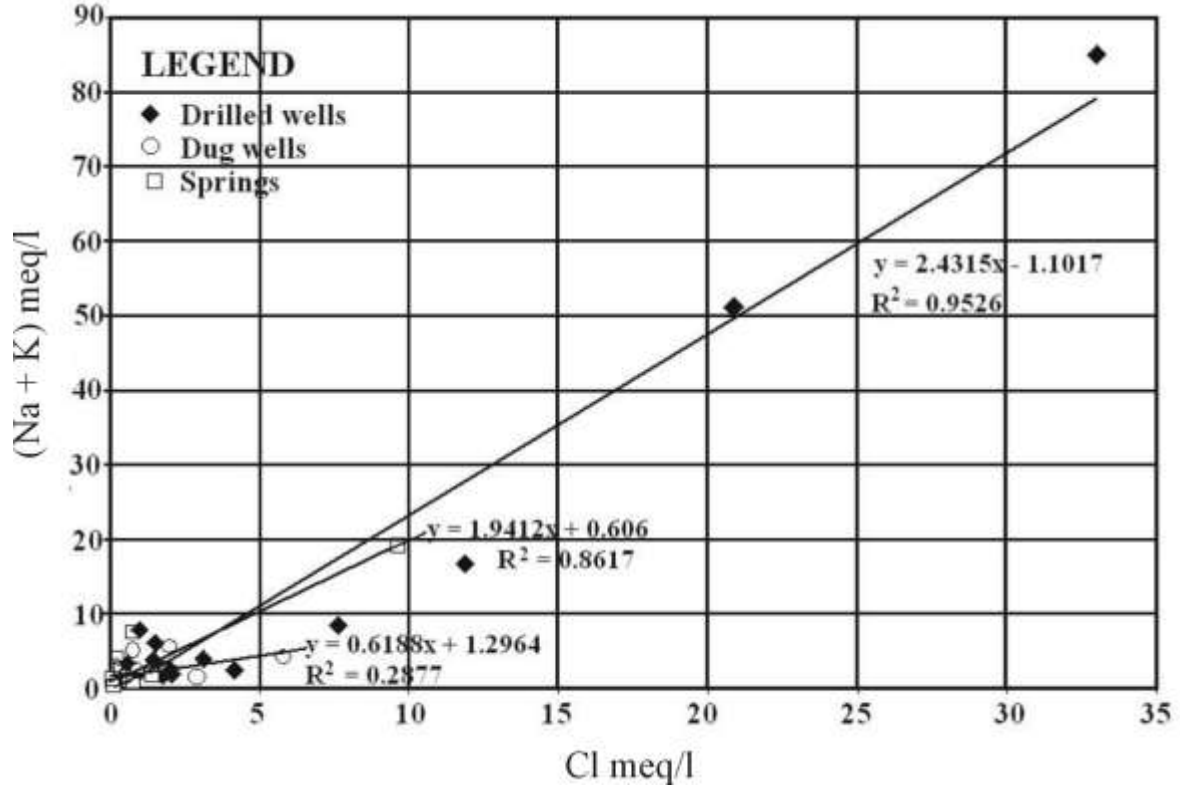

Fig. 7. Correlation between Cl and Na+K for all the water samples.

Table 4. Input parameters for hydrodynamic modeling of the Peshawar Basin using the FEMWATER code.

Parameter	Crystalline Rock	Upper Aquifer	Lower Aquifer	Confining Layer
Conductivity X (m/d)	0.03	3.0	2.0	0.01
Conductivity Y (m/d)	0.03	3.0	2.0	0.01
Conductivity Z (m/d)	0.01	1.0	0.75	0.005
Moisture content	0.25-0.31	0.35-0.43	0.35-0.43	0.15-0.20
Relative conductivity	0.15-0.50	0.25-1.0	0.25-1.0	0.11-0.31
Water capacity	0.0-0.19	0.0-0.03	0.0-0.03	
Young's Modulus (Pa)	$4x10^{10}$	$8x10^{10}$	$7x10^{10}$	$1x10^{10}$
Poisson's Ratio (Pa)	0.3	0.3	0.3	0.3
Compressibility (m^2/kg)	$4.3x10^{-12}$	$2.1x10^{-10}$	$1.5x10^{-10}$	$2.5x10^{-11}$

6. Hydrochemical geothermometry

In the present study, hydrochemical geothermometers (based on silica and cation abundances) were used to determine the source-reservoir temperatures for water samples from 34 springs (Table 3). The reservoir temperatures calculated for the S16 (emerging at the highest temperature of 67°C) using the silica geothermometers vary from $t_{(chalcedony)}$ = 75°C to $t_{(quartz)}$ = 105°C while the temperatures calculated with the cation geothermometer $t_{(Na\text{-}K\text{-}Ca)}$ = 84°C and cation geothermometer with Mg-correction $t_{(Na\text{-}K\text{-}Ca\text{-}Mg)}$ = 53.5°C. The temperatures calculated using lithium geothermometers are $t_{(Na\text{-}Li)}$ = 281°C and $t_{(Mg\text{-}Li)}$ = 119°C. The disparity between the resulting reservoir temperatures, and particularly the cation geothermometer with Mg-correction estimate falling below the measured orifice temperature of 67°C clearly indicate that at least one of the assumptions, most probably absence of mixing with cold water upon ascent from the reservoir to the surface is not fulfilled. This last conclusion is supported by strong relationship between the orifice temperature and silica concentrations and boron and lithium concentrations.

7. Numerical modeling parameters

Input parameters for the model include recharge, discharge, and bulk compressibility of the media and water. The ramping structures were used to mimic the field conditions and to incorporate lateral tectonic compression and weight of the imposed thrust sheets. The model is bounded on the east and south-east by the Indus River flowing from north to south. This constitutes a constant head (Dirichlet) boundary and nodal values of 1400 and 400 were assigned to the northern and southern end, respectively. The northern, western and south-western peripheries of the model were assigned no-flow boundaries, representing contact with the massive crystalline rocks of the thrust belts (Table 4). A constant flux (Neumann) boundary has been used to enter the recharge and evapotranspiration for the upper (unconfined) aquifer. Groundwater table was allowed to rise or fall accordingly, although no seasonal variations or unsaturated infiltration were modeled. Also, no attempt has been made to differentiate between the individual stratigraphic units within the respective sequences of formations. Instead, the stratigraphic section is highly simplified into four hydrostratigraphic units (Fig. 8; Table 4): 1. the upper unconfined aquifer corresponding to the Quaternary alluvial sediments and the uppermost, conglomeratic part of the Upper Siwalik; 2. the confining layer corresponding to the lacustrine sequence of the Upper Siwalik; 3. the confined aquifer corresponding to the lower conglomeratic part of the Upper Siwalik and the sandstone of the Middle Siwalik; and 4. crystalline rock.

Following definition of the conceptual model, including all the boundary conditions, sources/sinks, rainfall and seepage zones, and material properties within each of the layers a 3-D grid has been generated. The entire model was represented by 9200 nodes. 3-D representation of the model layers is shown on Fig. 8. The top (1) surface shows the surface topography viewed from southwest, towards northeast, towards the high Himalayas, with Peshawar Basin in the left-front. The horizontal line (2) represents an arbitrary datum surface. The surface (3) represents the top of the lacustrine sequence of the Upper Siwalik Formation (see Fig. 2), serving in the center part of the diagram as the base of the uppermost (unconfined) aquifer and top of the first confining layer. The lower surface (4) represents the bottom of the lower conglomeratic part of the Upper Siwalik and the sandstone of the Middle Siwalik, serving in the center part of the diagram as the base of the lower (confined) aquifer. Both surfaces plunge down stepwise to the east and west of the Peshawar Basin, reflecting the MMT and MCT (see Fig. 2). The values of hydraulic conductivity and compressibility were taken from published works such as Lisa et al., 1997 and Law et al., 1998. The convergence criteria for both the steady-state and transient simulations were set at 0.01 m. Recharge and discharge values for the basin are given in Table 5. Both deep and shallow wells have been represented in the model. Observation wells were installed to monitor the pressure heads and to provide a reliable tool for

calibration of the model. Model verification is not possible at this time, because the record of field measurements is not available for any previous time. However, any future measurements of the pressure heads can be used to verify this model. In a sensitivity analysis, the values of model parameters are varied across the range of likely values and the effect upon computed head is noted.

8. Modeling Results

Steady-state and transient simulations were performed for both topography-driven and tectonically-induced fluid flow conditions. Pressure head values in the wells range from 54 to 77 m above the screen depth (Table 6). Tectonic compression was imposed using the stair-step pattern and compressibility values for different layers. The distribution of pressure heads is uneven throughout the study area, but a general slope from north to south is evident in Fig. 8.

Transient simulations, with the stress increasing at 10,000 years time-intervals, show positive residuals of 0.98-2.90 m over the topography-driven flow at the last stress period of 100,000 years (Fig. 9; Table 6). An attempt was made to minimize these positive residuals by increasing the value of recharge to the model. As is evident from the sensitivity analysis, the model did not respond to higher values of recharge, and even doubling the recharge value did not minimize the positive residuals. It appears that the remaining positive residuals are aligned parallel to the major fault zones MMT and MCT (Fig. 8; Table 6). The successive transient simulations indicate that the residual pressure heads originate in the vicinity of these two major thrust zones in deeper horizons and gradually spread out to shallow levels. These residuals were minimized to a maximum of 0.35 m after incorporating the compressibility values (Table 6). It is our understanding that these positive residuals can only be caused by an additional force/pressure that cannot be explained by higher recharge or higher recharge-topography. Therefore, it is proposed that the requisite additional force derives from the litho-tectonic stress imposed by the compressional environment of the study area. In other words, results of the transient simulations appear to indicate that tectonic compression is responsible for the anomalous pressure heads observed in the area. Characteristically, pressure heads attain maximum values where the two fault zones (MMT, MCT) originate at depth (Fig. 9), suggesting that the higher than topographically-driven pressure heads are generated by influx of groundwater driven from deep aquifers by the confining tectonic pressure via the fault lines. Moreover - it appears that the new pressure heads attain their maximum values in the first two time steps, that is, within ~10^4-10^5 years.

Table 5. Recharge and discharge data for the Peshawar Basin (Robberts, 1988).

Recharge	**(Mm^3/yr)**	**Discharge**	**(Mm^3/yr)**
Precipitation	151	Baseflow	713
Surface water irrigation	734	Groundwater extraction	177
Groundwater-based irrigation	15	Evapotranspiration	1
Runoff	23		
Total	923		891

Table 6. Pressure head (P.H.) values (m) and the amount of residuals for the production and observation wells.

Node ID	**P.H. measured in field**	**Computed P.H. without consideration of compressibility**	**P.H. Residuals over Topography**	**Computed P.H. after inclusion of compressibility**	**Net Residuals**
4805	70	67.887	2.113	69.898	0.102
6727	65	62.669	2.331	63.903	1.097
5767	59	57.007	1.993	58.13	0.87
3845	54	53.013	0.987	53.358	0.642
3991	59	56.124	2.876	58.263	0.737
5913	76	73.1	2.9	74.667	1.333
4209	73	70.779	2.221	72.65	0.35
6131	62	60.046	1.954	61.17	0.83
4140	63	61.246	1.754	62.346	0.654
6062	57	55.51	1.49	56.38	0.62
4202	67	64.451	2.549	65.571	1.429
6124	77	75.139	1.861	78.519	-1.519
4464	61	58.109	2.891	62.668	-1.668

6386	73	70.216	2.784	71.594	1.406
4568	55	52.897	2.103	55.787	-0.787
6490	76	74.109	1.891	75.072	0.928

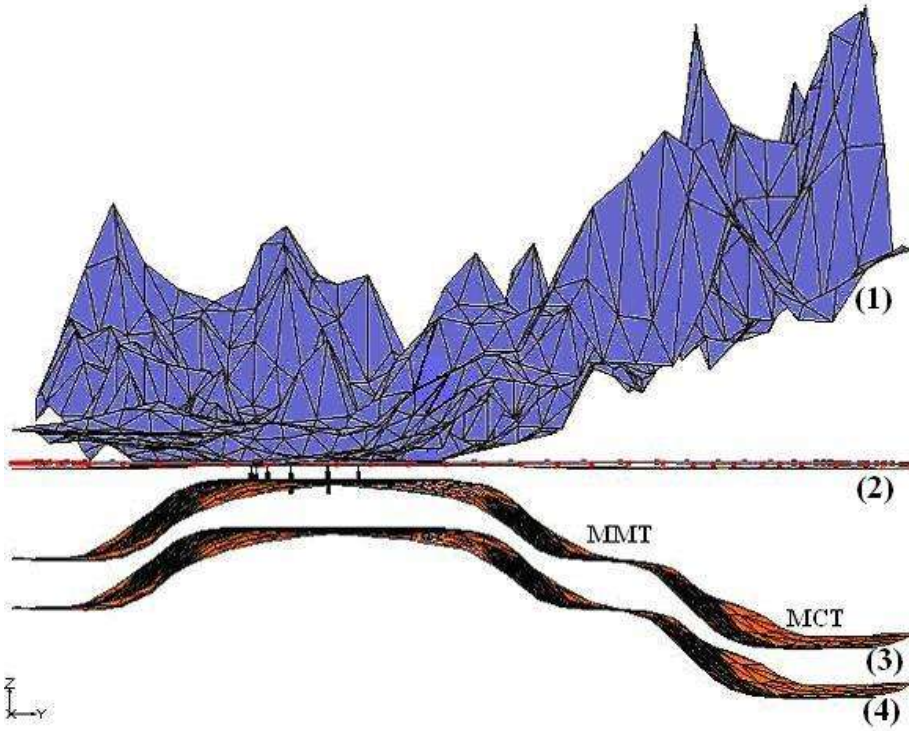

Fig. 8. 3-D diagram showing various layers of the numerical model.

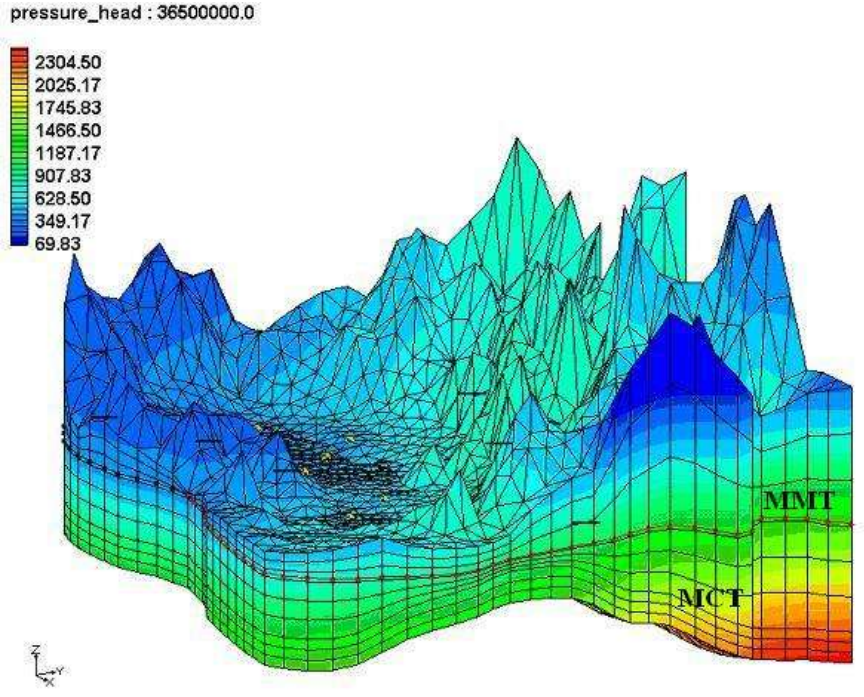

Fig. 9. Pressure head distribution after the transient simulation.

9. Discussion and conclusions

Results from water chemistry (Tables 1-3), in conjunction with the measured spring and water well temperatures and calculated reservoir temperatures for the spring water samples, combine to indicate that several of the sampling sites contain water with anomalous composition and temperature. Both characteristics suggest origin from deep horizons within the basin. Most of the groundwater samples show a significant elevated temperature over the local mean annual air temperature (see Tables 1-3). The elevated temperature is indicative of the fact that groundwater samples along the fault zones (MKT, MBT, and MCT) have gained excess heat, as compared to the groundwater samples more distant from the fault zones. All the groundwater samples reveal some signatures of mixing fresh recharge with the relatively old, deeply circulated waters (see Fig. 4). This trend can be clearly observed on the Piper (1944) diagram for spring water samples, where groundwater shows a spread along the HCO_3-SO_4 axis. Furthermore, all the samples with significantly high ΔT and anomalous composition have abnormally high concentrations of SiO_2, and the SiO_2 concentration of all the waters sampled along the major fault zones is higher than those sampled more distant from the fault zones. All of these anomalously high levels of components reflect initial dissolution of rock material by deeply circulating groundwater as it migrates to the shallower horizons sampled in this study. All these components indicate a positive correlation with the difference of water surface temperature and the local mean annual air temperature. The most pronounced positive correlation is obtained for SiO_2, indicating that high-temperature water dissolved more silica while circulating in the deeper formations. Boron and strontium are showing the same trend, although these trends are not as noticeable as that of the SiO_2 trend. The source reservoir temperature was calculated using silica and various cation geothermometers yielding widely ranging temperatures. However, assumption of the mixing system indicated by several bivariate chemical concentration and orifice temperatures narrows down the range of 116°C-155°C. Also, the reservoir temperature calculated using Mg-Li falls within this range. A probably less likely mixing model between the cold groundwater and hot fluids after steam separation yields the hot end member temperature of about 260°C. This model is less likely, because it implies adiabatic cooling of the ascending hot fluids, requiring rather unlikely rapid upflow of the hot fluids (Fournier, 1990) along the faultlines that are under compressive tectonic stress.

The Garam Chashma hot spring (S16) is the westernmost manifestation of the over 3000 km long Himalayan Geothermal Belt (HGB) between the MBT and MKT. The very high orifice temperature and anomalous composition of this hot spring cannot be explained by the simple fact that this water is gaining heat from the felsic plutons in the area. Moreover, these plutons are older than 5 Ma and are, therefore, considered too cold to contribute any heat to the descending recharge. Thus, the only contributing factor to the higher temperature of this hot spring appears to be the deeper circulation of groundwater and ascent through the fault zones. The topography-driven pressure from the highest ridges to the north of the study area may attain a maximum of 25 MPa as compared to the tectonic stress of 90 MPa. The question remains open as to which of these is prevalent for driving deep groundwater circulation. It is proposed here that the higher pressure regime is breaking the sealed thrusts in the foreland fold-and-thrust belt and adjoining areas.

Results of the numerical simulations point in the same direction. Results of the transient simulations indicate that topography alone is not sufficient to induce pressure heads observed in the field leaving substantially large positive residuals. Positive residuals are minimized when tectonic compression is incorporated as an input parameter. The positive residuals of 0.98-2.90 m are reduced to 0.40 m at the last stress period of the transient simulation, showing that tectonic compression is playing an important role in driving deep groundwater to the shallow levels observed in the water wells in the study area. The numeric calculations have shown also that tectonic compression can create periods of transient flows in foreland basins, with excess flow rates of the order of 10^{-4} to 10^{-3} m/yr for thrust sheet loads from 1 to 10 km thick. Most of the excess pressure generated by compression appears to dissipate in about 10^4 to 10^5 years before a new steady state can be reached in about 10^4 to 10^5 years. Ge and Garven (1992) arrived at the same conclusion for the Arkoma basin in central Arkansas and Oklahoma.

Also, a substantial amount of heat is presumably generated by frictional movement along these faults (Todaka et al., 1988). Finally, the remarkable proximity of the anomalously high pressure heads (Fig. 9) and all the thermal and hydrochemical anomalies (Yousafzai et al., this issue) to the major overthrust faults support the hypothesis that waters with anomalous composition and temperatures in the Peshawar basin ascended from greater depths along the major fault lines (MMT, MBT and MKT). Although overthrust faults are usually tightly sealed with cataclastic or mylonitized breccias such as the MMT (Dipietro et al., 2000; Singh, 2003), thus rendering them impervious to groundwater flow, it would seem that the overall tectonic pressure within the basin is high enough to overcome this obstacle. It is, therefore, proposed here that the higher pressure regime

is breaking the sealed by fault breccias thrust-lines in the foreland fold-and-thrust belt and adjoining areas.

Acknowledgments

The authors gratefully acknowledge financial support from Geological Society of America, and Sigma Xi in conducting fieldwork for this research. Department of Geology at Kent State University facilitated analytical and computational procedures. The authors are indebted to Dr. Ksenija Dejanovic for her priceless help in carrying the chemical analyses.

References

Bitzer, K., Trave, A., Calvet F., Labaume, P., 1996. Modeling fluid flow and heat transport in compressive sedimentary basins: application to the Ainsa basin. Geogaceta, 20, 1369-1371.

Deming, D., Nunn, J.A., Evans, D.G., 1990. Thermal effects of compaction-driven groundwater flow from overthrust belt. Journal of Geophysical Research, 95, 6669-6683.

Dipietro, J.A., Ahmad I., Hussain, A., 2000. The Main Mantle Thrust in Pakistan; its character and extent. Geological Society Special Publications, 170, 375-393.

Evans, M.J., Derry, L.A., Anderson, S.P., France-Lanord, C., 2001. Hydrothermal source of radiogenic Sr to Himalayan rivers. Geology, 29, 803-806.

Fournier, R.O., 1990. The interpretation of Na-K-Mg relations in geothermal waters. Geothermal Resource Contribution and Transactions, 14, 1421-1425.

Garven, G., 1995. Continental-scale groundwater flow and geologic processes. Annual Reviews of the Earth and Planetary Sciences, 23, 89-117.

Ge, S., Garven, G., 1992. Hydromechanical modeling of tectonically driven groundwater flow with application to the Arkoma foreland basin. Journal of Geophysical Research, 97, 9119-9144.

Ge, S., Garven, G., 1994. A theoretical model for thrust-induced deep groundwater expulsion with application to the Canadian Rocky mountains. Journal of Geophysical Research, 99, 13851-13868.

Hussain, A., Dipietro, J.A., Pogue, K.R., 1998. Stratigraphy and structure of the Peshawar Basin, Pakistan. Journal of Nepal Geological Society, 18**,** 25-35.

Hochstein, M.P., Yang, Z., 1995. The Himalayan Geothermal Belt (Kashmir, Tibet, West Yunnan). In: Gupta, M.L., Yamamo, M. (Eds.), Terrestrial Heat Flow and Geothermal Energy in Asia. Oxford and IBH Publishing Co. New Delhi, 331-368.

Law, B.E., Shah, S.H.A., Malik, M.A., 1998. Abnormally high formation pressures, Potwar Plateau, Pakistan. In: Law, B.E., Ulmishek, G.F., Slavin, V.I. (Eds.), Abnormal Pressures in Hydrocarbon Environments. AAPG Memoir, 70, 247-258.

Lisa, M., Ghazi, G.R., Hashmi, S., Jadoon, I.A.K., Khwaja, A.A., 1997. Nature of faults and focal mechanism solutions of part of northern Pakistan. Geological Bulletin, University of Peshawar, 30, 143-151.

McPherson, B.J.O.L., Garven, G., 1999. Hydrodynamics and overpressure mechanisms in the Sacramento Basin, California. American Journal of Science, 299, 429-466.

Nakata, T., 1989. Active faults of the Himalaya of India and Nepal. Geological Society of America Special Paper, 232, 243-264.

Neuzil, C.E., 1995. Abnormal pressures as hydrodynamic phenomena. American Journal of Science, 295, 742-786.

Oliver, J., 1986. Fluids expelled tectonically from orogenic belts: their role in hydrocarbon migration and other geologic phenomena. Geology, 14, 99-102.

Piper, A.M., 1944. A graphical procedure in the geochemical interpretation of water-analysis. American Geophysical Union Transactions, 25, 914-923.

Pivnik, D.A., Sercombe, W.J., 1993. Compression- and transpression-related deformation in the Kohat Plateau, NW Pakistan. Geological Society Special Publication, 74, 559-580.

Rathur, A.Q., 1987. Groundwater management to eradicate water logging and salinity in the Upper Indus Basin, Punjab, Pakistan. In: Awadalla, S. (Ed.), Proceedings of the International Conference on Groundwater and Environment. Kebangsaan University, Selangor, G96-G107.

Robberts, J.H., 1988. Groundwater in the Peshawar Valley, Peshawar District, Mardan District and Malakand Agency. NWFP Technical Report V-2, WAPDA Hydrogeology Directorate Peshawar and TNO Institute of Applied Geoscience, Delft, The Netherlands.

Singh, B.P., 2003. Evidence of growth fault and forebulge in the Late Paleocene (~57.9-54.7 Ma), western Himalayan foreland basin, India. Earth and Planetary Science Letters, 216, 717-724.

Todaka, N., Shuja, T.A., Jamiluddin, S., Khan, N.A., Pasha, M.A., Iqbal, M., 1988. A preliminary study for Geothermal Development Project in Pakistan. Geological Survey of Pakistan, 4–47.

Wandrey, C.J., Law, B.E., 1999. Map showing geology, oil and gas fields, and geologic provinces of South Asia. USGS Open File Report, 97-470C, Version 2.0 (CD-ROM).